Effective Synergism Between WO_3 and *g*-C_3N_4 Nanostructures towards Efficient Visible-Light-Driven Photocatalytic Application

Mohammad Ehtisham Khan*

Department of Chemical Engineering Technology, College of Applied Industrial Technology (CAIT), Jazan University, Jazan 45971, Kingdom of Saudi Arabia

***Corresponding author**: Mohammad Ehtisham Khan (mekhan@jazanu.edu.sa)*

Abstract

The development of tungsten oxide-graphitic carbon nitride nanostructures as a photocatalyst using (W-g-CN) nanostructures has proven simple and efficient. It showed a considerable improve in photocatalytic competence as assessed with bare g-C3N4 and WO3 when used to degrade the dyes methylene blue and Rhoda mine B under visible light. Analytical techniques were used to characterize the nanostructures as fabricated. As matched to bare WO3 and bare g-C3N4, the nanostructures' evident performance was 3.65 times higher and 3.72 times higher, respectively. This performance was much higher than the results reported previously. Additionally, nanostructured samples were evaluated for their optical properties. In nanocomposite samples, the bandgap is in the range of 2.3–2.5 eV, which facilitates the deprivation of dyes under visible light irradiation. A detailed explanation is offered for how the WO3–g-C3N4 photocatalyst may be able to achieve higher catalytic efficiency. In addition to advanced optical absorption at the visible region and appropriate positions of band in W-g-CN nanostructures, the enhanced performance was found to be due to synergistic influences between the g-C3N4 and WO3 nanostructures interfaces.

Keywords: graphitic carbon nitride; tungsten oxide, facile method, visible light, dye degradation

Introduction

Solar energy can be converted into chemicals through photocatalysis, an appealing yet challenging method for reducing energy consumption and addressing environmental issues [1]. In the field of photocatalysis, efficiency, simplicity, and sustainability are key challenges [2, 3]. Because TiO2 nanoparticles are non-toxic, stable, and excellent photocatalysts, they are the most commonly used semiconductor photocatalysts [4-7]. It has an excellent photogenerated electron–hole pair recombination rate, however, it has two main shortcomings: a poor conversion rate of solar energy and a minimal conversion rate of photo-generated electron–hole pairs [8, 9]. The performance of TiO2 is excellent, but its application in industry is inadequate [10, 11]. The future of photocatalysts will require high visibility, high performance, and chemical stability.

It has been reported by Mishra *et al*. that graphitic carbon nitride (g-C3N4) is a stable and considered as a non-metal catalyst [12]. Water splitting and organic pollutant decomposition under visible light are ideal uses for this material, which comprised a band gap of 2.7 eV [13, 14]. Despite its high photo-generated electron–hole pairs, g-C3N4 has a low photocatalytic efficiency that is constrained by its high rate of recombination [15, 16]. Several techniques have been utilized to increase the photocatalytic performance of g-C3N4 including nanostructure, metal deposition, nonmetallic doping, protonation, and other combinations. [13, 15-20]. These strategies significantly improved the catalytic performance of g-C3N4 and extended its application opportunities by including functional elements or groups into its matrix or adding functional groups to its surface. Photocatalytic and optical absorption properties of g-C3N4 are improved when visible light is irradiated on it. The catalytic activity of g-C3N4 can be further optimized using examining other appropriate compounds.

Photoinduced electron-hole pairs could be separated by semiconductor coupling and the activity of photocatalytic systems can be improved [21]. Tungsten oxide (WO3) is a potential alternative photocatalyst with a wide range of applications, including transducing energy, deactivating viruses, and degrading hazardous pollutants. [2, 5, 22]. It is also worth mentioning that the band gap energy of WO3 nanostructures lies within the solar spectrum (about 2.7–2.8 eV), so it can be used in visible light applications [23, 24]. Its photocatalytic activity is limited by its conduction band edge, which is disapproving of single electron reduction of O2 during visible light irradiation. This prevents the photocatalyst from degrading organic matter under O2 conditions [25]. In present years, several efforts have been made to enhance photocatalytic performance of WO3, such as controlling its size, improving its morphology, depositing noble metals upon it, and coupling it with other semiconductors in order to enhance its photocatalytic activity [2, 25-29]. A study has shown that WO3 makes semiconductor heterojunctions with higher photocatalytic performance [30]. WO3 has been described to couple with semiconductors [30-32] to form heterostructure photocatalysts with advanced photocatalytic implementation under visible illumination [31, 32]. The polymeric g-C3N4 photocatalyst created when combined with WO3 provides an efficient photocatalytic performance under visible light. The obtained WO3-g-C3N4 (W-g-CN) nanostructures are therefore a favorable nanostructured material for photocatalysis [33].

We have fabricated novel W-g-CN nanostructures by hydrothermal means as photocatalysts. Various techniques were used to characterize the photocatalysts, including XRD, DRS, PL, XPS, and HR-TEM. A detailed investigation and discussion of the photocatalytic deprivation of organic waste product was conducted using the (W-g-CN) nanostructures system. Additionally, a possible mechanism to enhance (W-g-CN) nanostructures' photocatalytic activity was proposed.

2. Experimental

2.1 Materials and methods

The reagents were bought from Sigma-Aldrich, Samchun, J. T. Baker and Kojima Chemicals, Japan which were used without further purification. BARE ROUP 30 water purification technique which was used throughout the fabrication process. Other chemicals, urea and oxalic acid were acquired from Samchun, Korea,

while C_2H_6O was purchased from J. T. Baker. Tungsten hexachloride (WCl_6) and methylene blue (dye) Rhodamine B (dye) were purchased from Sigma-Aldrich.

2.2 Preparation of photocatalyst

In the first step, graphitic g-C3N4 was prepared in a muffle furnace under air flow conditions by moderately heating urea at 550 °C for 4 h with 20 °C min-1 ramping rate [34]. A sheet-like composition of bare g-C3N4 was extracted as a whitish yellow powder after the resultant material was physically cooled off at room temperature.

The WCl6 (99.99%) was gradually dissolved in 40 mL of ethanol and the oxalic acid solution together gently stirred at room temperature to achieve a consistent solution in a typical manufacturing process [25]. The obtained solution was then stirred using magnetic stirrer, while 0.46 g of urea was gradually included. An autoclave tube lined with Teflon was placed in a power-driven oven at 200°C for 24h after stirring the precursor solution for 20 minutes. As soon as the precipitate had been obtained, the sample was splashed with a certain ethanol and de-ionized water several times and dried up in an oven at 60°C overnight. Desiccators were used to store the nano-powder until further characterization could take place.

Finally, 50 mg of the as-prepared WO3 nano-powder was combined to 40 mL of ethanol in a beaker. In the next step, 20 mg of carbon nitride nano-powder was included to the solution and treated with ultrasonic waves for 1.5 hours. Transferring the solution into an autoclave tube lined with Teflon and keeping it at 200°C for 12 hours was done. Several washes with absolute ethanol and deionized water were performed after the reaction was completed, and the product was dried out at 60°C for one day. In order to characterize the as-prepared sample further, the WO3 nanorods together with graphitic carbon nitride were stored as WO3 nanorods–graphitic carbon nitride nanostructures (W-g-CN).

2.3 Characterization

An X-ray diffraction analysis using Cu Ka radiation (λ= 1.5405 nm) at the PANalytical X'pert PRO-MPD in The Netherlands. According to the JCPDS data file, the crystalline phases exhibited excellent XRD matching to the standard compounds. A diffuse absorbance spectrophotometer (VARIAN, Cary 5000, USA) was used to examine the optical properties. A 325 nm excitation wavelength was used to measure the photoluminescence of the samples (PL, Kimon, 1 K, Japan). X-ray photoelectron spectroscopy (XPS, ESCALAB 250 XPS System, Thermo Fisher Scientific U.K.) was performed at the Center for Research Facilities, South Korea, using monochromate Al Ka radiation with 15kV, 150W, 500mm spot size, 90 °C take-off angle, 20 eV pass energy, 0.6 eV BE resolution. In order to examine the microstructure of Au 3d5, a transmission electron microscope (FE-TEM, Tecnai G2 F20, FEI, USA) operating at a voltage of 200 kV was used. An electron microscope was used for observing both high angle spherical dark fields (HAADF) and designated-area electron diffraction (SAED). The TEM equipped with energy dispersive spectrometers (EDS) were used to perform quantitative analysis.

2.4 Photocatalytic measurements

MB dye and RhB degradation were assessed underneath visible light to determine the photocatalytic functioning of the samples. 100mL of MB (100 mg) or RhB4 (100 mg) water put in a beaker with 100 mg photocatalyst. We evaluated the sample's photocatalytic activity under a 400 W lamp at 31 mW cm2 (3M, > 400 nm, USA).

Magnetic stirring was performed in the dark for about 30 minutes prior to irradiation to ensure that photocatalysts and dye particles obtained an equilibrium of adsorption-desorption. In order to remove the particles of the photocatalyst, 3 mL aliquots were taken at certain intervals and centrifuged. As a second step, the UV-Vis spectra of MB were measured using a spectrophotometer (UV-2450 Shimadzu). Since 663 nm is the maximum absorption band of MB, the variations in its UV-vis spectrum were examined. The following formula was used to find out the degradation efficiency of MB and RhB by photocatalysis [35]:

$$E = \left(1 - \frac{C}{C_0}\right) \times 100\% = \left(1 - \frac{A}{A_0}\right) \times 100\% \quad \text{(i)}$$

In this equation, C is the MB solution concentration at time t, C0 is the equilibrium concentration of MB after adsorption-desorption (at time 0), and A and A0 are the absorbance values of MB at the same period. A UV-vis spectrophotometer (OPTIZEN 2120UV) was also used to determine Rhodamine B concentration.

3. Results and discussions

3.1. Analysis of WO_3-g-C_3N_4 (W-g-CN)

3.1.1. Standard characterization of W-g-CN nanostructures

Analysis of the structural, and phase verification of bare W-g-CN nanostructures and g-C3N4 nanostructures

A simple hydrothermal method is used to synthesize WO3 and g-C3N4 distinctly by hydrothermal methods. In Figure 1 a, X-ray diffraction analysis was conducted to study the crystal structure, and purity of g-C3N4. It was seen that g-C3N4 revealed two distinct peaks on its XRD pattern at 13.1°and 27.3° 2θ. The minor peak at 13.1° 2θ which was allotted to the (100) plane with d = 0.676 nm and the supplementary peak at 27.3° 2θ resembled to d = 0.324 nm owing to the long-array interplanar amassing the arrangement of aromatic and it is predictable as the (002) plane of bare *g*-C_3N_4 (JCPDSD 87-1526) [36, 37]. As shown in Figure 1, (b), all samples of WO3-g-C3N4 nanostructures exhibit similar XRD patterns. Accordingly, the major peak of WO3 was significantly shifted from its earliest position after addition of g-C3N4 and appeared with a decreased intensity in all samples [38]. The WO3-g-C3N4 nanostructures did not have any peaks of g-C3N4, which could be owed to the actual low point strength of g-C3N4 in comparison to bare WO3. In the meantime, bare WO3 has a stronger peak than bare g-C3N4, so when it was combined with g-C3N4 to achieve the nanostructure, the peak of bare g-C3N4 could not be seen. It is also intriguing that the samples do not contain g-C3N4. As the primary peak of *g*-C_3N_4 centered at 27.11 lies concerning the two WO_3 peaks located at 26.81 and 28.17 corresponding to (101) and (110) planes, respectively. Nanostructure samples with very small d-spacing intervals will never reveal the g-C3N4 peak. Accordingly, the presence of g-C3N4 can be confirmed from Fig. 1(c). An individual can clearly see the presence of WO3 in all the samples by looking at the major peaks of the samples altogether. Fig. 1 (c) EDX spectrum of W-g-CN composite nanostructures. There is no sign of impurities in the as-prepared composite since it contains only C, N, O and W elements.

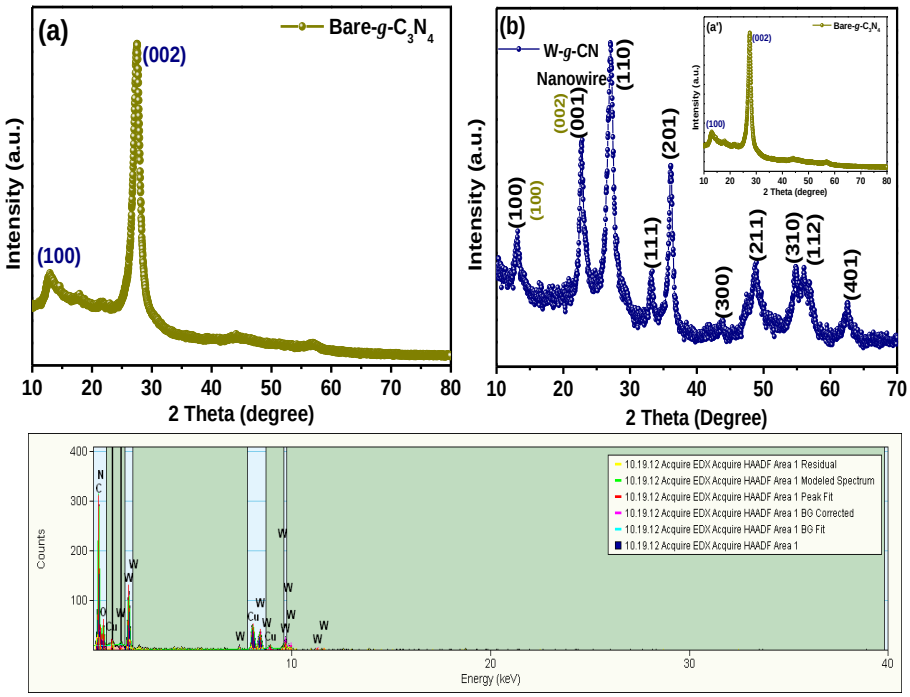

Figure 1. XRD patterns of g-C3N4, W-g-CN, and EDX spectrums of W-g-CN nanostructures.

3.1.2. Optical absorption analysis of W-*g*-CN nanostructures

Furthermore, WO3, g-C3N4 nanostructures were analyzed for their absorption spectra as revealed in Figure 2. According to figure 2, the edge of absorption from bare WO3 corresponds to nearby 400 nm, while that of bare C3N4 corresponds to near 410 nm. In composite samples, g-C3N4 introduced into WO3 initiates the edge of absorption shift concerning the extensive wavelength range, as illustrated in Figure 2.[39]. Decreased band gaps were caused by this changing of absorption edges. In nanostructures, the smaller band gap allows them to absorb more energy, which leads to a greater integer of electrons moving from the valence bands to the conduction bands [39]. Therefore, the performance as a catalyst will be progressed by producing more electron-hole pairs between the two semiconductors.

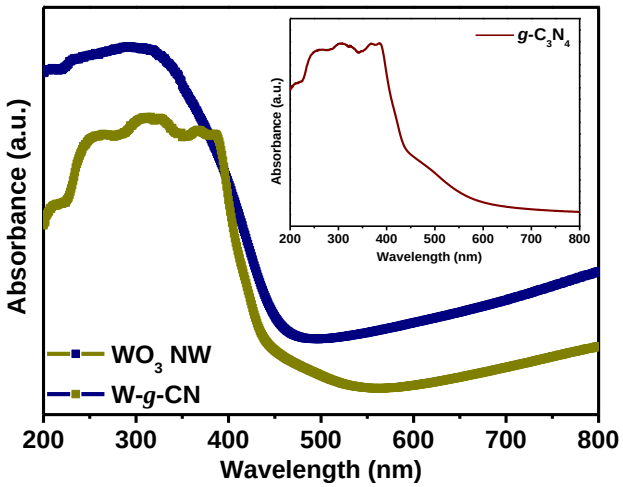

Fig. 2 UV-Visible absorbance spectra of WO_3 and W-*g*-CN nanostructures.

In order to recognize the providence of electrons and holes in nanostructures, we can examine the PL bands of the W-g-CN nanostructure [39, 40]. Fig. 3 indicates the PL peaks of bare g-C3N4, bare WO3, and W-g-CN nanostructures. Due to their corresponding band gaps, the g-C3N4 and WO3 each have peaks at nearby 460 nm.

Based on figure 3, the release strength of the PL spectra for the composite of WO3 and g-C3N4 declined upon addition of g-C3N4 sheets, which revealing a depleted rate of recombination from photogenerated charge carriers in the complex of WO3 and g-C3N4. [39]. Compared to other samples, the intensity of has the least crystal defects, while the intensity of has the most defects [39]. During the recombination process, the crystal defects proceed as a center of recombination for holes and as well for electrons. With the addition of WO3 nanocrystals, the PL spectra of the W-g-CN nanostructures showed a significant reduction in emission intensity, and the order of composites matched the photocatalytic activity, suggesting a much lower rate of charge carrier recombination in the nanostructures.

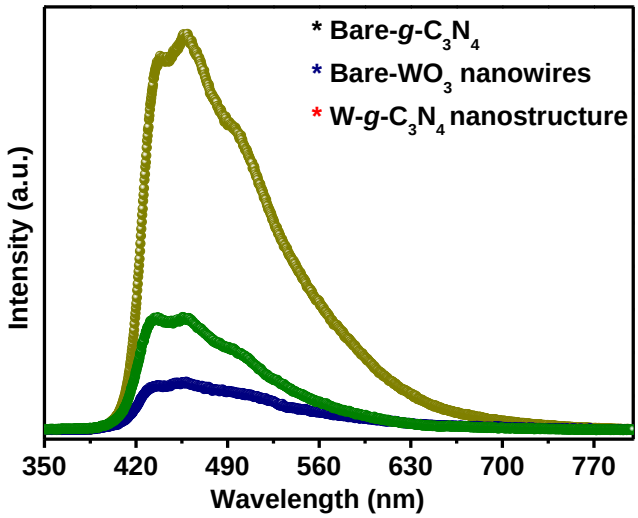

Fig. 3. The photoluminescence spectra of bare *g*-C_3N_4, bare WO_3 and W-*g*-CN nanostructures.

3.1.3. XPS analysis of W-*g*-CN nanostructures

In XPS, the chemical environment and oxidation status of an element are confirmed by observing X-ray photoelectron spectroscopy (XPS).. In the region, W-g-CN nanostructures were subjected to XPS at 0–1000 eV (Fig. 4).

Accordingly, the W-g-CN nanostructures as prepared were analyzed using XPS for formal oxidation states [41]. It was evident from Figure 4 (a) that the fabricated samples were free of impurities since they contained three major peaks for C, N, and O, a small peaks for WO3, and no other peaks for any other element [41]. As can be seen in Figure 4(b), the C 1s peaks are located at 285 eV and 288.3 eV, respectively, and these are associated with the hybridized sp2 carbon atom and with the hybridized carbon atom connected to trinity nitrogen atoms - C(N3) of the g-C3N4. According to Fig. 4 (c), N 1s has a broad fit peak of 398.5 eV attributed to nitrogen atoms linked to dual carbon atoms (C–N–C),

whereas the smaller close-fitting peaks were associated with nitrogen atoms bonding to triad carbon atoms, N–(C3), and N–H bonds. The O1s peak (Fig. 4 (d)) associated with the WO3 is centered at 530.5 eV.. Figure 4 (d) shows the binding energies for W4f7/2 and W4f5/2 at 35.5

eV and 35.7 eV, respectively. According to the literature, these values are very close to those reported by XPS [42]. It was observed that W4f7/2 and W4f5/2 binding energies in the 9.7% WO3/g-C3N4 composite were 35.3 and 37.5 eV, respectively, which are marginally inferior than those in bare WO3. The edge between WO3 and g-C3N4 may be responsible for such a shift.

So, graphitic carbon nitride sp2-bonded to graphite is confirmed. It has been proposed that the peaks at 400.5 eV and 404.8 eV are caused by tertiary nitrogen (N–(C)3) groups and the effect of the charging process [40]. Consequently, the results of the combined XRD, DRS, PL, TEM, and XPS investigations confirmed the heterojunction structure was composed of both WO3 and g-C3N4.

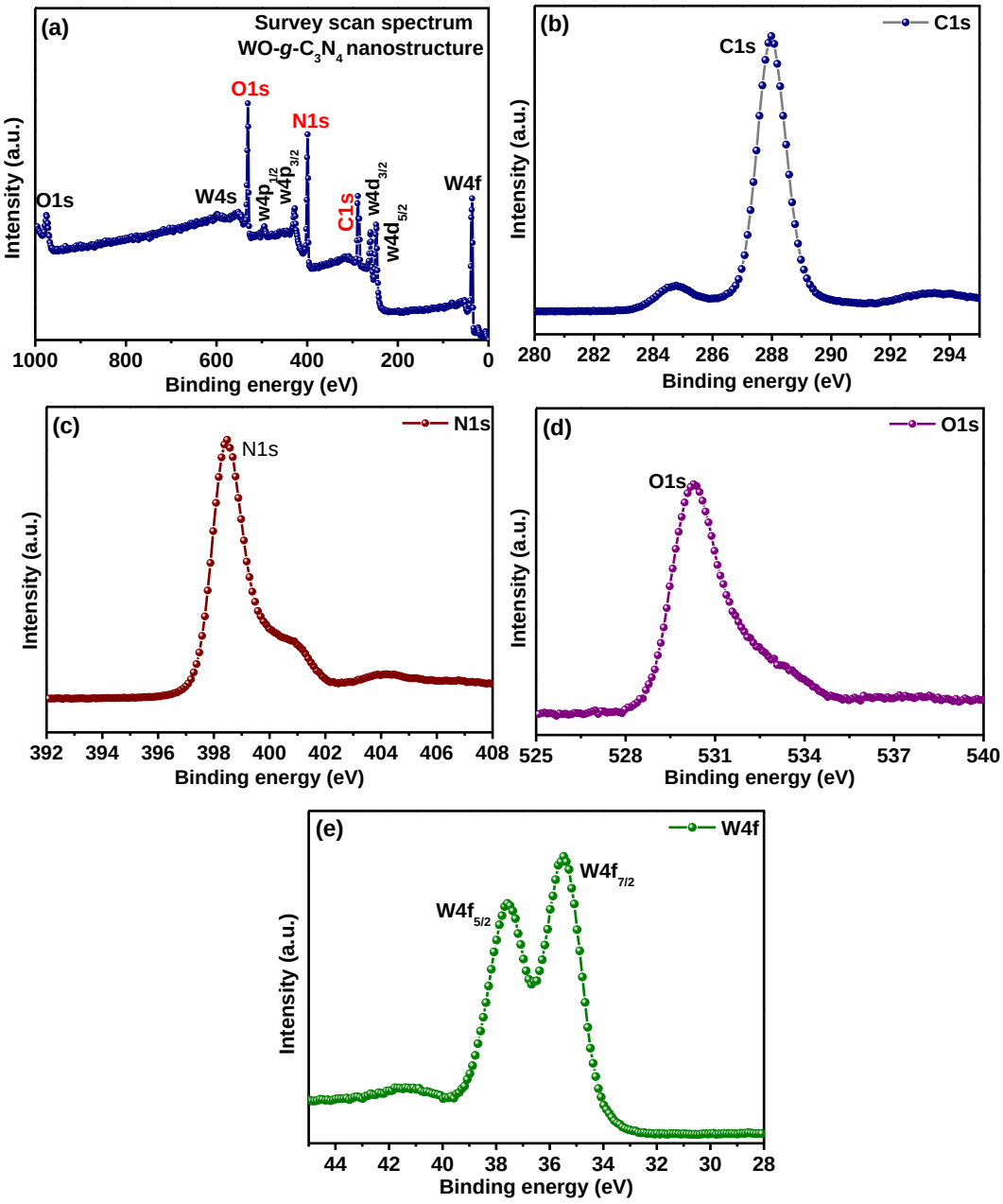

Fig. 4. The XPS profile of the W-g-CN nanostructure **(a)** Scan spectra, **(b)** C1s spectra (c) N1s Spectra **(d)** O 1s spectra and, **(e)** High resolution spectra of the W4f peak W-g-CN nanostructure.

3.1.4. Morphological analysis of W-*g*-CN nanostructure

As shown in Fig. 5 (a - e), TEM and HR-TEM were used to examine the surface morphology of W-g-CN nanostructure[40]. Various rod shapes are illustrated in Figure 5 (a) at various scaling levels on the surface of carbon nitride nanosheets. A further confirmation of this was provided by elemental mapping, which demonstrated that the WO3 nanorods are encapsulated within the carbon nitride nanosheets.

In addition to TEM and EDS analyses, WO3 nanorods–carbon nitride nanostructures were also characterized by their morphology and composition. As can be seen in figure 5(a), due to the two-dimensional disposition of the sheet, the carbon nitride sheet shows an abundance of rod-shaped structures. The TEM images clearly show the placement of WO3 nanorods on the carbon nitride nanosheets as well as the intimate contact between them. The HR-TEM image in Figure 5(b) illustrates the direct interaction between WO3 nanorods and carbon nitride nanosheets, as well as the interfacial interaction between WO3 nanorods and carbon nitride nanosheets. According to Figure 5(c-d), the WO3 nanorods have a 0.36 nm spacing between their lattices and fringes. As can be seen in the inset of Figure 5 (c), the SAED pattern showed that the WO3 was polycrystalline. To further confirm the lattice fringes in the nanostructures prepared, figure 5 (d) shows HR-TEM images at 5 nm scale. A similar elemental mapping is shown in Figure 5 (e' - e''''), which further confirms the existence of each element. Carbon nitride nanosheet surfaces were found to be successfully anchored and covered with WO3 nanorods, as determined through TEM and HE-TEM analyses.

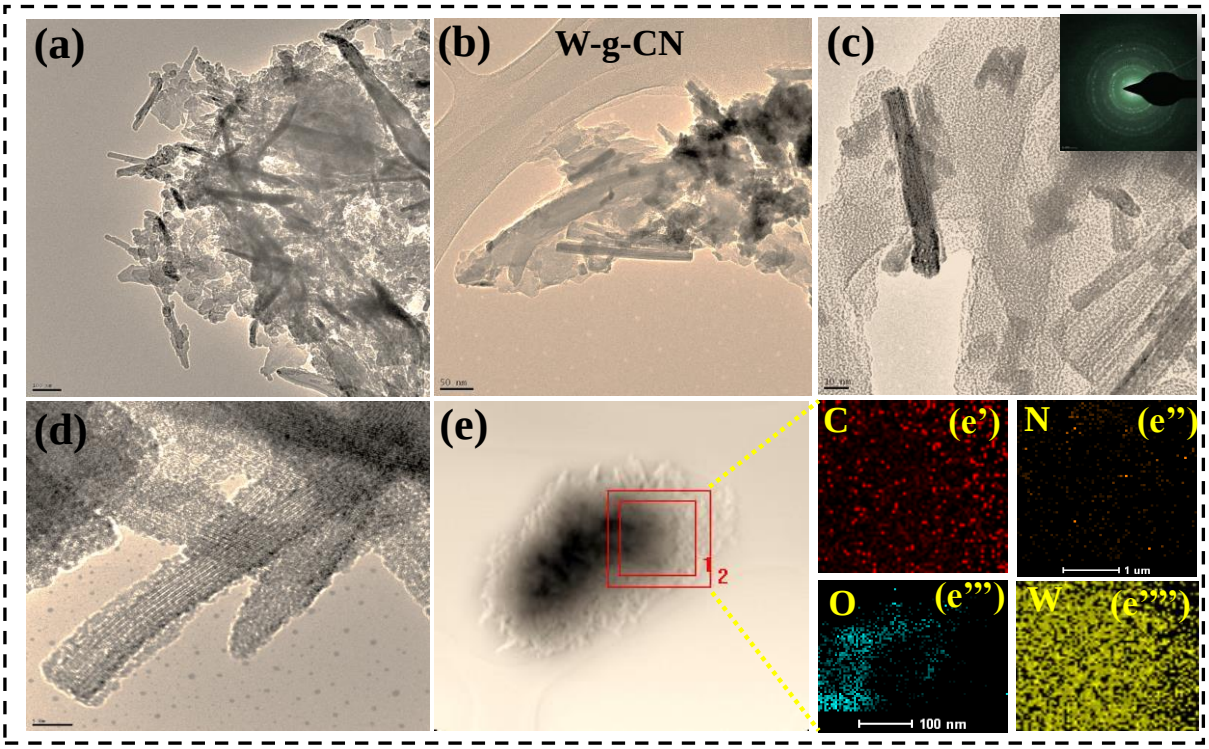

Fig. 5 Images of WO3 nanorods-carbon nitride nanostructures obtained with TEM (a) The presence of WO3 nanorods on carbon nitride sheets, (b) TEM image of WO3 nanorods interacting with carbon nitride sheets, (c) SAED pattern on the lattice fringes of WO3 nanorods under HR-TEM, (d) To confirm fringes, HR-TEM image at 5 nm scale was taken, (e) The area selected for the elemental mapping (e'-e'') of C, N, O, and W was mapped.

4. Testing the stability of nanostructures made of WO3/g-C3N4 and their photocatalytic implementation

As part of the photocatalytic evaluation, methylene blue and Rhodamine B were decomposed using W-g-CN nanostructures irradiated by visible light [43]. A photocatalytic activity measurement was performed using bare g-C3N4, bare WO3 and the as-prepared W-g-CN nanostructures as photocatalysts. The self-degradation of MB was almost nonexistent without the presence of a photocatalyst[43]. A certain level of photodegradation was observed under visible light for the bare g-C3N4 and bare WO3 in the present research. A bare g-C3N4 catalyst and a bare WO3 catalyst could degrade MB by 41% and 76%, respectively, after 3 hours. Compared to bare g-C3N4 and bare WO3 nanostructures, all W-g-CN nanostructures showed high photocatalytic activity by >98% [42].

Under visible light irradiation, RhB photodegrades successfully. Figure 6 (b) illustrates the degradation of RhB solution. As time goes by, the absorption peak increases, indicating successful photodegradation.

A comparison between W-g-CN nanostructures and bare g-C3N4 and WO3 reveals that W-g-CN nanostructures have a much higher photocatalytic capability [44]. In terms of degrading contamination, photocatalysts display the best performance. Using the Langmuir-Hinshelwood model, the first-order equation of the model is used to promote photocatalytic reactions of contaminants in aqueous solutions:

$$\ln(Ci/C0) = kt \qquad \text{(ii)}$$

The concentration of organic dye at time t is Ci, while the concentration of initial dye is C0. This is a plot of ln(Ci/C0) for the catalysts versus the irradiation time t in figure 6(b).
Compared to bare g-C3N4, bare WO3, and all W-g-CN nanostructures, all W-g-CN nanostructures have higher rate constants k.

Some factors reportedly contributed to RhB's poor photodegradation performance; the surface agglomeration of nanoparticles may affect the catalyst's efficiency [45, 46]. There is a possibility that high nanoparticle content in heterojunction could significantly affect dispersion and cause the nanoparticles to agglomerate, which could result in the homojunction structure being totally destroyed [47]. This directed to a reduce in photocatalytic performance of the samples with a higher WO3 content because electrons and holes were less efficiently separated from one another. As a consequence, the W-g-CN nanostructures must contain a appropriate ratio and dispersal of WO3 in direct to increase the endeavor of g-C3N4. A noteworthy observation was that the combination sample did not seem to improve g-C3N4 photocatalytic performance, indicating that the WO3 and g-C3N4 interactions after calcination might have an important role in advancing the degradation performance. As a result of both WO3 and g-C3N4 improving the photocatalytic activity, WO3 and g-C3N4 exhibited synergistic effects in photocatalytic degradation of MB and RhB under visible light.

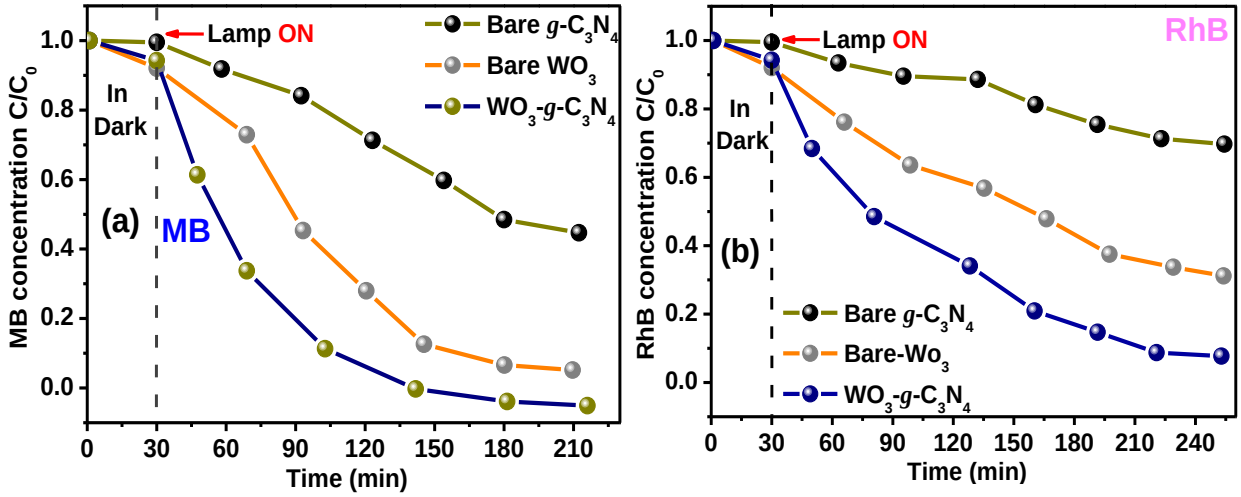

Fig. 6 (a and **b)** A plot of C/C0 with respect to time (h) for the deprivation of MB and RhB under photoreaction.

In order to evaluate the photocatalytic properties of the sample, W-g-CN nanostructures were suspended in water and sonicated for 1 hour to evaluate their photocatalytic constancy. In Figure 7 (a), the suspension consisted entirely of W-g-CN nanostructures with no WO3 leaching out, proving the stability of W-g-CN nanostructures as better catalysts. After three cycles under the same conditions, both the fabricated W-g-CN nanostructure and g-C3N4 nanostructure displayed good reusability (Figure 7b). During the recycling process, catalyst loss is expected, resulting in the slight decrease observed.

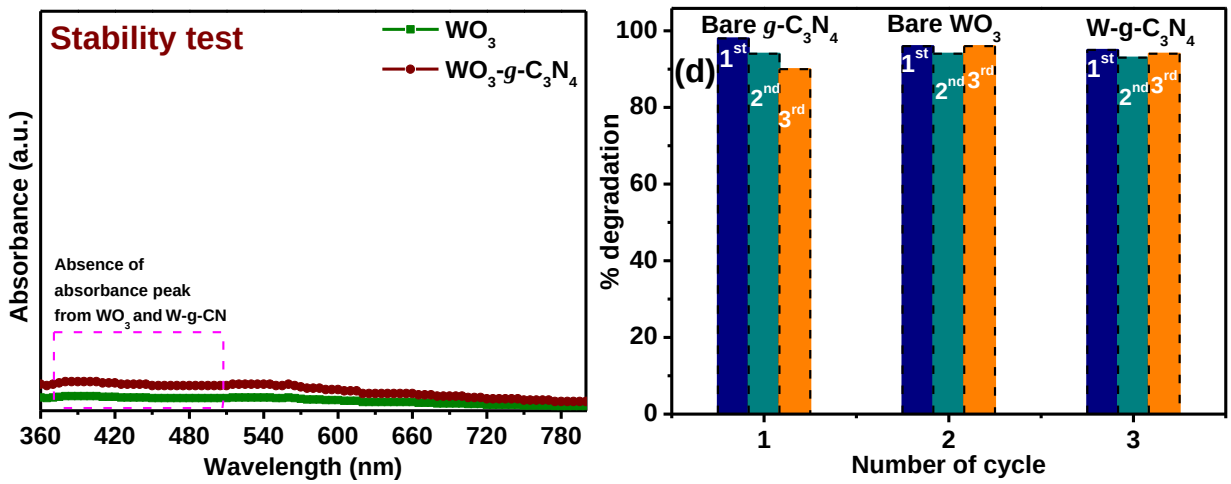

Fig. 7 (a) The stability tests and **(b)** the reusability tests of bare *g*-C_3N_4, bare WO_3 and W-g-CN nanostructures.

5. Possible photocatalytic mechanism

When visible light is irradiated on g-C3N4 and WO3, electrons will transition from VB to CB in both semiconductors [48]. The photogenerated holes transfer from the VB levels of WO3 to the VB levels of C3N4 since g-C3N4 has a negative VB level and WO3 has a positive CB potential. In the meantime, the photoexcited electrons in the CB of g-C3N4 could move to the CB of WO3. It is possible for these electrons to react with WO3 species to reduce W6+ to W5+ by reacting with the WO3 species. Through a reaction with oxygen, the W5+ ions on the surface of WO3 could be re-oxidized into W6+, generating superoxide radicals (•O2).[48]. In addition to forming superoxide, superoxide radicals can also form water radicals (•OH) by reacting with H2O molecules [49]. A visible light irradiated RhB is degraded primarily into CO2 and H2O by hydroxyl radicals (OH) and superoxide radicals (O2). Accordingly, both g-C3N4 and WO3 coupling reduce or oxidize photoinduced holes and electrons to increase separation efficiency in composite surfaces under visible light illumination.

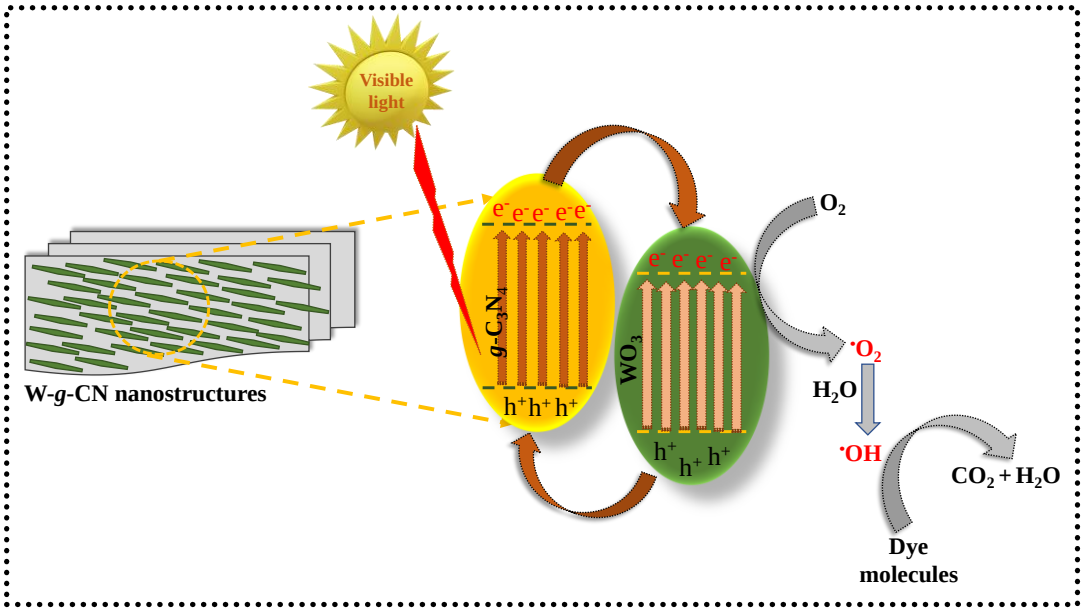

Fig. 8 A possible degradation mechanism for photocatalysts in the existence of visible light.

6. Conclusions

W-g-CN nanostructure synthesis was accomplished over a facile hydrothermal approach. It is important to treat the sheets with 400 °C in order to obtain uniformly dispersed WO3 nanorods. By increasing reaction sites under visible light illumination, increasing visible light absorption, and restraints of electron-hole recombination, the photocatalytic performance is enhanced. It was determined that W-g-CN nanostructures displayed the best degradation activity against MB and RhB. As a result, the major active groups in the photocatalytic structure are radicals from hydroxyl (•OH) and radicals from superoxide (•O2). It is thus demonstrated here how W-g-CN nanostructures can be readily fabricated and used to improve the photocatalytic degradation process. A new method to fabricate high-performance photocatalysts for environmental remediation applications is of potential importance for degradation of pollutants through W-g-CN nanostructures.

Declaration of competing interest

The authors declare that they have no known competing financial interests or personal relationships that could have appeared to influence the work reported in this paper.

Acknowledgements

The authors extend their appreciation to the Deputyship for Research & Innovation, Ministry of Education in Saudi Arabia

References

[1] H. Zhou, Y. Qu, T. Zeid, X. Duan, Towards highly efficient photocatalysts using semiconductor nanoarchitectures, Energy & Environmental Science, 5 (2012) 6732-6743.

[2] L. Huang, H. Xu, Y. Li, H. Li, X. Cheng, J. Xia, Y. Xu, G. Cai, Visible-light-induced WO 3/gC 3 N 4 composites with enhanced photocatalytic activity, Dalton Transactions, 42 (2013) 8606-8616.

[3] Y. Qu, X. Duan, Progress, challenge and perspective of heterogeneous photocatalysts, Chemical Society Reviews, 42 (2013) 2568-2580.

[4] H.N.C. Dharma, J. Jaafar, N. Widiastuti, H. Matsuyama, S. Rajabsadeh, M.H.D. Othman, M.A. Rahman, N.N.M. Jafri, N.S. Suhaimin, A.M. Nasir, A Review of Titanium Dioxide (TiO2)-Based Photocatalyst for Oilfield-Produced Water Treatment, Membranes, 12 (2022) 345.

[5] M.S.S. Danish, L.L. Estrella, I.M.A. Alemaida, A. Lisin, N. Moiseev, M. Ahmadi, M. Nazari, M. Wali, H. Zaheb, T. Senjyu, Photocatalytic applications of metal oxides for sustainable environmental remediation, Metals, 11 (2021) 80.

[6] M.E. Khan, M.M. Khan, B.-K. Min, M.H. Cho, Microbial fuel cell assisted band gap narrowed TiO2 for visible light-induced photocatalytic activities and power generation, Scientific reports, 8 (2018) 1-12.

[7] A. Mohammad, M.E. Khan, M.H. Cho, T. Yoon, Fabrication of binary SnO2/TiO2 nanocomposites under a sonication-assisted approach: Tuning of band-gap and water depollution applications under visible light irradiation, Ceramics International, 47 (2021) 15073-15081.

[8] W. Li, Z. Wu, J. Wang, A.A. Elzatahry, D. Zhao, A perspective on mesoporous TiO2 materials, Chemistry of materials, 26 (2014) 287-298.

[9] F.W. Low, C.W. Lai, Recent developments of graphene-TiO2 composite nanomaterials as efficient photoelectrodes in dye-sensitized solar cells: A review, Renewable and Sustainable Energy Reviews, 82 (2018) 103-125.

[10] M.J. Gázquez, J.P. Bolívar, R. García-Tenorio García-Balmaseda, F. Vaca, A review of the production cycle of titanium dioxide pigment, (2014).

[11] D. Chen, Y. Cheng, N. Zhou, P. Chen, Y. Wang, K. Li, S. Huo, P. Cheng, P. Peng, R. Zhang, Photocatalytic degradation of organic pollutants using TiO2-based photocatalysts: A review, Journal of Cleaner Production, 268 (2020) 121725.

[12] A. Mishra, A. Mehta, S. Basu, N.P. Shetti, K.R. Reddy, T.M. Aminabhavi, Graphitic carbon nitride (g–C3N4)–based metal-free photocatalysts for water splitting: a review, Carbon, 149 (2019) 693-721.

[13] M. Ismael, Y. Wu, A mini-review on the synthesis and structural modification of gC 3 N 4-based materials, and their applications in solar energy conversion and environmental remediation, Sustainable Energy & Fuels, 3 (2019) 2907-2925.

[14] A. Mohammad, M.E. Khan, M.R. Karim, M.H. Cho, T. Yoon, Ag-modified SnO2-graphitic-carbon nitride nanostructures for electrochemical sensor applications, Ceramics International, 47 (2021) 23578-23589.

[15] C. Prasad, H. Tang, Q. Liu, I. Bahadur, S. Karlapudi, Y. Jiang, A latest overview on photocatalytic application of g-C3N4 based nanostructured materials for hydrogen production, international journal of hydrogen energy, 45 (2020) 337-379.

[16] G. Mamba, A. Mishra, Graphitic carbon nitride (g-C3N4) nanocomposites: a new and exciting generation of visible light driven photocatalysts for environmental pollution remediation, Applied Catalysis B: Environmental, 198 (2016) 347-377.

[17] M.R. Rajeshwari, S. Kokilavani, S.S. Khan, Recent developments in architecturing the g-C3N4 based nanostructured photocatalysts: Synthesis, modifications and applications in water treatment, Chemosphere, (2021) 132735.

[18] M.E. Khan, T.H. Han, M.M. Khan, M.R. Karim, M.H. Cho, Environmentally sustainable fabrication of Ag@ g-C3N4 nanostructures and their multifunctional efficacy as antibacterial agents and photocatalysts, ACS Applied Nano Materials, 1 (2018) 2912-2922.

[19] A. Mohammad, M.R. Karim, M.E. Khan, M.M. Khan, M.H. Cho, Biofilm-assisted fabrication of Ag@ SnO2-g-C3N4 nanostructures for visible light-induced photocatalysis and photoelectrochemical performance, The Journal of Physical Chemistry C, 123 (2019) 20936-20948.

[20] A. Mohammad, M.E. Khan, M.H. Cho, Sulfur-doped-graphitic-carbon nitride (Sg-C3N4) for low cost electrochemical sensing of hydrazine, Journal of Alloys and Compounds, 816 (2020) 152522.

[21] H. Tang, S. Chang, L. Jiang, G. Tang, W. Liang, Novel spindle-shaped nanoporous TiO2 coupled graphitic g-C3N4 nanosheets with enhanced visible-light photocatalytic activity, Ceramics International, 42 (2016) 18443-18452.

[22] G. Jeevitha, R. Abhinayaa, D. Mangalaraj, N. Ponpandian, Tungsten oxide-graphene oxide (WO3-GO) nanocomposite as an efficient photocatalyst, antibacterial and anticancer agent, Journal of Physics and Chemistry of Solids, 116 (2018) 137-147.

[23] O. Samuel, M.H.D. Othman, R. Kamaludin, O. Sinsamphanh, H. Abdullah, M.H. Puteh, T.A. Kurniawan, WO3–based photocatalysts: A review on synthesis, performance enhancement and photocatalytic memory for environmental applications, Ceramics International, (2021).

[24] P. Shandilya, S. Sambyal, R. Sharma, P. Mandyal, B. Fang, Properties, optimized morphologies, and advanced strategies for photocatalytic applications of WO3 based photocatalysts, Journal of Hazardous Materials, (2022) 128218.

[25] M.E. Khan, M.M. Khan, M.H. Cho, Fabrication of WO 3 nanorods on graphene nanosheets for improved visible light-induced photocapacitive and photocatalytic performance, RSC advances, 6 (2016) 20824-20833.

[26] A.M. Mohammed, S.S. Mohtar, F. Aziz, S.A. Mhamad, M. Aziz, Review of various strategies to boost the photocatalytic activity of the cuprous oxide-based photocatalyst, Journal of Environmental Chemical Engineering, 9 (2021) 105138.

[27] S.Z. Hussain, M. Ihrar, S.B. Hussain, W.C. Oh, K. Ullah, A review on graphene based transition metal oxide composites and its application towards supercapacitor electrodes, SN Applied Sciences, 2 (2020) 1-23.

[28] L. Cui, X. Ding, Y. Wang, H. Shi, L. Huang, Y. Zuo, S. Kang, Facile preparation of Z-scheme WO3/g-C3N4 composite photocatalyst with enhanced photocatalytic performance under visible light, Applied Surface Science, 391 (2017) 202-210.

[29] A.T. Doan, X.D.N. Thi, P.H. Nguyen, V.N.N. Thi, S.J. Kim, V. Vo, Graphitic gC 3 N 4-WO 3 composite: synthesis and photocatalytic properties, Bulletin of the Korean Chemical Society, 35 (2014) 1794-1798.

[30] K. Sivula, R. Van De Krol, Semiconducting materials for photoelectrochemical energy conversion, Nature Reviews Materials, 1 (2016) 1-16.

[31] T.S. Natarajan, R.J. Tayade, Photocatalysis: Present, past and future, Inorganic Pollutants in Wastewater: Methods of Analysis, Removal and Treatment, 16 (2017) 1.

[32] Z. Chao, Study on Water Purification Using Tungsten Trioxide Photocatalyst under Visible Light, (2012).

[33] X. Han, D. Xu, L. An, C. Hou, Y. Li, Q. Zhang, H. Wang, WO3/g-C3N4 two-dimensional composites for visible-light driven photocatalytic hydrogen production, International Journal of Hydrogen Energy, 43 (2018) 4845-4855.

[34] A. Mohammad, M.E. Khan, M.R. Karim, M.H. Cho, Synergistically effective and highly visible light responsive SnO2-g-C3N4 nanostructures for improved photocatalytic and photoelectrochemical performance, Applied Surface Science, 495 (2019) 143432.

[35] R. Fazaeli, H. Aliyan, S. Tangestaninejad, S. Parishani Foroushani, Photocatalytic degradation of RhB, MG, MB, Roz.B, 3-BL and CI-50 by PW12-APTES@MCF as nanosized mesoporous photocatalyst, Journal of the Iranian Chemical Society, 11 (2014) 1687-1701.

[36] L. Ge, C. Han, J. Liu, In situ synthesis and enhanced visible light photocatalytic activities of novel PANI–g-C3N4 composite photocatalysts, Journal of Materials Chemistry, 22 (2012) 11843-11850.

[37] A. Mohammad, M.E. Khan, T. Yoon, M. Hwan Cho, Na,O-co-doped-graphitic-carbon nitride (Na,O-g-C3N4) for nonenzymatic electrochemical sensing of hydrogen peroxide, Applied Surface Science, 525 (2020) 146353.

[38] C. Cheng, J. Shi, Y. Hu, L. Guo, WO₃/g-C₃N₄ composites: one-pot preparation and enhanced photocatalytic H₂ production under visible-light irradiation, Nanotechnology, 28 (2017) 164002.

[39] A. Priya, R.A. Senthil, A. Selvi, P. Arunachalam, C.K. Senthil Kumar, J. Madhavan, R. Boddula, R. Pothu, A.M. Al-Mayouf, A study of photocatalytic and photoelectrochemical activity of as-synthesized WO3/g-C3N4 composite photocatalysts for AO7 degradation, Materials Science for Energy Technologies, 3 (2020) 43-50.

[40] L. Huang, H. Xu, Y. Li, H. Li, X. Cheng, J. Xia, Y. Xu, G. Cai, Visible-light-induced WO3/g-C3N4 composites with enhanced photocatalytic activity, Dalton Transactions, 42 (2013) 8606-8616.

[41] V. Alman, K. Singh, T. Bhat, A. Sheikh, S. Gokhale, Sunlight Assisted improved photocatalytic degradation of rhodamine B using Pd-loaded g-C3N4/WO3 nanocomposite, Applied Physics A, 126 (2020) 724.

[42] K. Mallikarjuna, M.K. Kumar, H. Kim, Synthesis of oxygen-doped-g-C3N4/WO3 porous structures for visible driven photocatalytic H2 production, Physica E: Low-dimensional Systems and Nanostructures, 126 (2021) 114428.

[43] H. Vijeth, S.P. Ashokkumar, L. Yesappa, M. Vandana, H. Devendrappa, Photocatalytic degradation of methylene blue and Rhodamine B using polythiophene nanocomposites under visible and UV light, AIP Conference Proceedings, 2115 (2019) 030536.

[44] X. Zhang, X. Lu, Y. Shen, J. Han, L. Yuan, L. Gong, Z. Xu, X. Bai, M. Wei, Y. Tong, Y. Gao, J. Chen, J. Zhou, Z.L. Wang, Three-dimensional WO3 nanostructures on carbon paper: photoelectrochemical property and visible light driven photocatalysis, Chemical Communications, 47 (2011) 5804-5806.

[45] V. Subramanian, E.E. Wolf, P.V. Kamat, Catalysis with TiO2/Gold Nanocomposites. Effect of Metal Particle Size on the Fermi Level Equilibration, Journal of the American Chemical Society, 126 (2004) 4943-4950.

[46] H. Xu, J. Yan, Y. Xu, Y. Song, H. Li, J. Xia, C. Huang, H. Wan, Novel visible-light-driven AgX/graphite-like C3N4 (X=Br, I) hybrid materials with synergistic photocatalytic activity, Applied Catalysis B: Environmental, 129 (2013) 182-193.

[47] J. Lu, I. Do, L.T. Drzal, R.M. Worden, I. Lee, Nanometal-decorated exfoliated graphite nanoplatelet based glucose biosensors with high sensitivity and fast response, ACS nano, 2 (2008) 1825-1832.

[48] J. Meng, J. Pei, Z. He, S. Wu, Q. Lin, X. Wei, J. Li, Z. Zhang, Facile synthesis of g-C3N4 nanosheets loaded with WO3 nanoparticles with enhanced photocatalytic performance under visible light irradiation, RSC Advances, 7 (2017) 24097-24104.

[49] I. Aslam, C. Cao, M. Tanveer, W.S. Khan, M. Tahir, M. Abid, F. Idrees, F.K. Butt, Z. Ali, N. Mahmood, The synergistic effect between WO3 and g-C3N4 towards efficient visible-light-driven photocatalytic performance, New Journal of Chemistry, 38 (2014) 5462-5469.